Appendix

Bound within Boundaries: How Well Do Protected Areas Match Movement Corridors of Their Most Mobile Protected Species?

David D. Hofmann[1,§,*]   Dominik M. Behr[1,2,*]   John W. McNutt[2]

Arpat Ozgul[1]   Gabriele Cozzi[1,2]

July 9, 2020

[1] Department of Evolutionary Biology and Environmental Studies, University of Zurich, Winterthurerstarsse 190, 8057 Zurich, Switzerland.

[2] Botswana Predator Conservation Trust, Private Bag 13, Maun, Botswana.

[§] Corresponding author (david.hofmann2@uzh.ch)

[*] Shared first authorship

Running Title: Connectivity across a Transfrontier Conservation Area.

Keywords: dispersal, habitat selection, integrated step selection function, Kavango-Zambezi Transfrontier Conservation Area, landscape connectivity, least-cost corridors, Lycaon pictus, permeability surface, protected areas, wildlife management
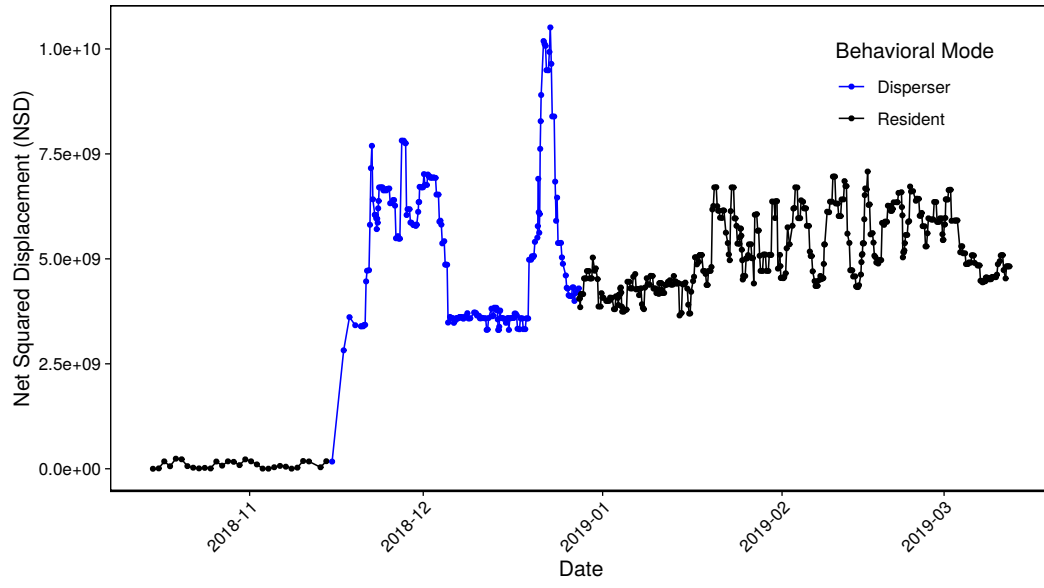
A.1   Net Squared Displacement

Figure S1: NSD displacement through time for one of our dispersers. The blue line indicates the period during which we calssified the individual as dispersing.
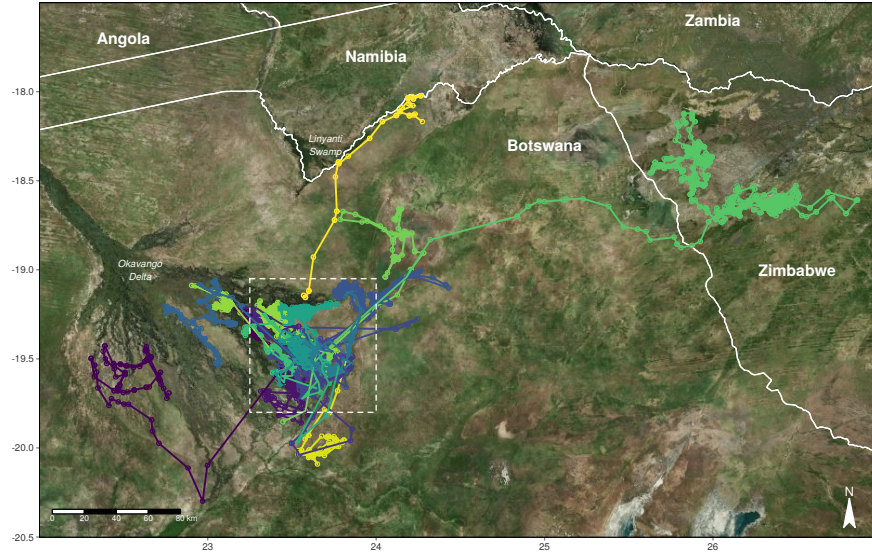
A.2 GPS Data

Figure S2: Illustration of all trajectories that we recorded. Each color represents a different dispersing coalition. All coalitions departed from the area which is indicated by the white dashed rectangle. The coalition dispersing towards the far east of the map covered over 360 km in under 10 days. Satellite background imagery was provided by Microsoft Bing.

Table S1: Summary statistics of all GPS relocations that have been recorded on dispersing coalitions.

Coalition ID	Sex	Pack Affiliation	# Fixes Total	# Fixes During Dispersal	# Days Dispersing	Euclidean Dispersal Distance (in km)	Cumulative Dispersal Distance (in km)
Abel	M	MU	894	45	9	131	205
Amacuro	F	MB	954	583	137	23	1'090
Belgium	M	ZU	1'097	158	28	18	319
Dalwhinnie	F	PA	545	62	22	50	243
Denali	F	MN	1'096	173	33	11	528
Everest	M	MN	389	123	38	67	572
Kalahari	F	HT	1'753	467	130	20	1'963
Karisimbi	M	MN	438	141	34	45	251
Liuwa	F	AP	946	92	19	144	451
Lupe	M	KW	2'209	396	34	8	436
MadameChing	F	AP	776	729	136	263	1'560
Mirage	M	HT	814	182	36	7	435
Odzala	M	AP	1'410	205	42	53	412
Scorpion	M	KB	2'676	393	34	4	471
Stetson	M	MT	384	383	33	3	481
Taryn	F	AP	896	37	9	10	130

A.3   Spatial Covariates

To investigate habitat preferences of dispersing wild dogs, we used a set of geo-referenced covariates that we aggregated in the categories *land cover*, *protection status*, and *human influence*. We did not include terrain features as covariates due to the absence of noteworthy elevational gradients in our study area. For each covariate, we prepared spatial raster layers from freely available online services or from remotely sensed satellite imagery. To ensure a consistent resolution (i.e. cell-size or grain) across covariates, we coarsened or interpolated all layers to match a resolution of 250m x 250m. We performed processing and manipulation of data as well as all spatial and statistical analyses using R, version 3.6.1 (R Core Team, 2019).

A.3.1   Land Cover

A.3.1.1   Water

The covariate water included rivers, wetlands, and swamps. Because the inundation extent of the flood in the Okavango Delta is highly variable within and between years, we created dynamic "flood maps" that were updated every 8th day following a remote sensing algorithm developed by the Okavango Research Institute (ORI; Wolski et al., 2017). To implement the algorithm, we defined two sets of polygons located in the region of the Okavango Delta (Figure S3). The first set consisted of areas known to be permanent dryland, whereas the second set consisted of permanent waters. Since we were unable to retrieve the original polygons used in Wolski et al. (2017), we geo-referenced and digitized the polygons reported in their publication. After recreating the polygons, we used the R-package *getSpatialData* (Schwalb-Willmann, 2018) to download and pre-process all relatively cloud-free MODIS Terra images (MCD43A4; Schaaf and Wang, 2015) available for the period of our dispersal events. Assessment of cloud cover was based on visual inspection of MODIS images on ORI's website (`www.okavangodata.ub.bw/ori/monitoring/flood_maps`). After download, we classified each MODIS image into a binary map of water (flood) and dryland using a threshold that was identified as follows. First, we extracted all reflectance values of MODIS Terra Band 7 within the water- and dryland-polygons. Second, we computed histograms of water-reflectances and dryland-reflectances and empirically verified that reflectances of the two groups were sufficiently distinct. More specifically, we checked if superimposing the histograms of water-reflectances and dryland-reflectances resulted in a bimodal histogram. This was said to be achieved if the 99th percentile of water-reflectances did not severely

exceed the 1st percentile of dryland-reflectances ($p_{0.99,water} - \frac{10}{255} < p_{0.01,dryland}$). Third, if bimodality was achieved, we calculated a threshold (t) using Equation S1:

$$t = \widetilde{p}_{water} + 0.3 * (\widetilde{p}_{dryland} - \widetilde{p}_{water}) \qquad \text{(Equation S1)}$$

where $\widetilde{p}_{water}$ and $\widetilde{p}_{dryland}$ were the median reflectances of water and dryland, respectively. We then classified all pixels of MODIS Terra Band 7 with a value greater than t as dryland and all pixels with a value smaller than t as water.
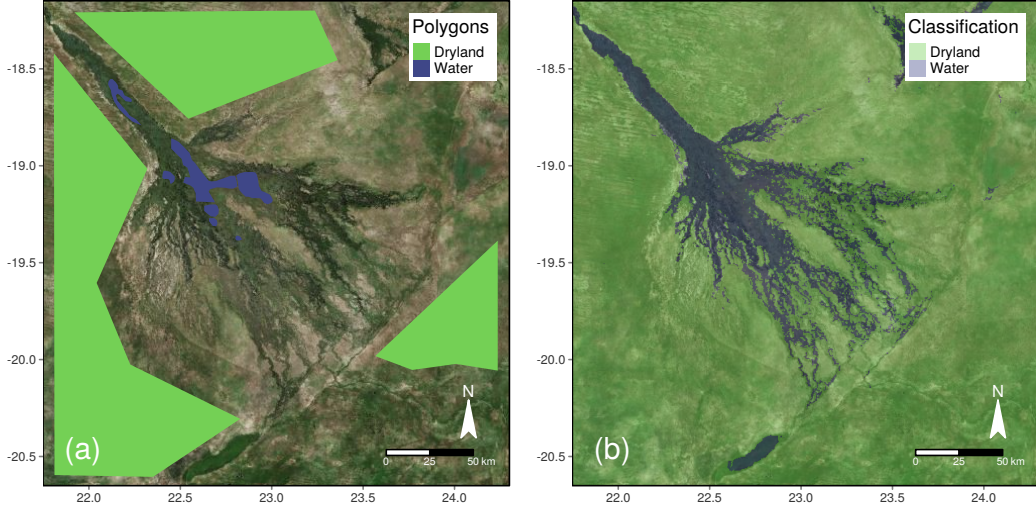

Figure S3: Images describing the flood mapping algorithm. (a) The colored polygons indicate permanent waters (blue) and permanent dryland (green). Below these polygons we extracted reflectance values of MODIS Terra Band 7 and used their repsective medians to calculate a classification threshold t. (b) Example of a classified MODIS Terra Band 7 image after application of the threshold. The satellite image in the background was provided by Microsoft Bing.

Importantly, bimodality was not always achieved and in some cases no flood map could be calculated. In fact, it appears that non-bimodality caused the ORI algorithm to fail since the end of 2018, which is why no flood maps have been generated since then (ORI, personal comm.). We hypothesized that this was caused by the application of static water-polygons that did not cover permanent waters correctly anymore. Therefore, we revised the algorithm and allowed for a more dynamic polygonization of water. That is, for each MODIS image we calculated new water-polygons comprising areas that were covered by the flood in 99% of the flood maps from the previous five years. All of the necessary flood maps from previous years were kindly provided to us by ORI. Using this slightly amended approach, we were able to address some of the bimodality issues and to classify several additional flood maps for the period of our study. Because MODIS Terra Band 7 had a resolution of 500m x 500m, we interpolated all maps to 250m x 250m.

To validate and compare the performance of our own algorithm to the original ORI-algorithm, we randomly sampled 48 dates for which ORI prepared classified images. To make sure that months were equally represented in the sampled dates, we employed stratified sampling based on months (regardless of the year) and randomly sampled four maps for each month. For the sampled dates we downloaded and classified MODIS Terra Band 7 images and compared our classified images to those provided by ORI (Figure S4). For each pair of maps we created a difference map indicating false positives and false negatives and computed the relative number of wrongly classified pixels. We achieved an overall accuracy of 97%, which presumably is an underestimate of the true performance, as we introduced some errors when resampling the ORI-maps to our reference grid.
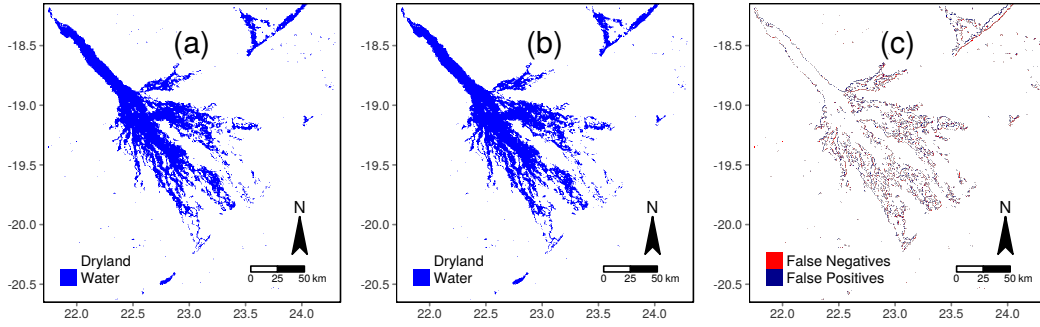

Figure S4: Validation procedure of our flood mapping algorithm. (a) Classified image that was provided to us by ORI. (b) Image for the same date but now classified using our own algorithm. (c) Difference image indicating false positives and false negatives in our own classification.

While we created dynamic flood maps for the Okavango Delta, we assumed the extent of all other water bodies (e.g. Chobe river, Zambezi river) to be static within and between years. This static representation was based on Globeland's land cover dataset (Chen et al., 2015), from which we only retained the categories *wetland* and *water bodies* and collectively reclassified them to *water*. Globeland had an original resolution of 30m x 30m, so we coarsened the layer to 250m x 250m using the mode of each 250m x 250m cell. We further improved river representation by employing the rasterized MERIT Hydro dataset (Yamazaki et al., 2019) from which we added all rivers with a width of over 10m to our Globeland layer. We merged dynamic and static water maps into a large rasterstack, covering the entire study area. We also created a rasterstack rendering the covariate *distance to water* by calculating the Euclidean distance of each raster cell in the study area to the nearest source of water.

A.3.1.2 Dryland

We subdivided dryland into three layers as derived from the MODIS Terra Vegetation Continuous Fields dataset (MOD44B; Dimiceli et al., 2015). The three layers depicted percent-

age cover of tree-vegetation (henceforth *trees*), non-tree-vegetation (henceforth *shrubs/grassland*), and non-vegetated (henceforth *bare land*) and added up to 100% of dryland coverage. We used our flood map that aligned with the creation date of these MODIS layers and defined anything covered by water as 0% vegetated. The MODIS vegetation layers had a resolution of 250m x 250m and no coarsening or interpolation was required.

A.3.2 Protection Status

We created a binary layer separating protected from unprotected land. We downloaded corresponding data on protection status in shapefile format from the Peace Parks Foundation (`www.peaceparks.org`; Peace Parks Foundation, 2019). Protected areas included forest reserves, game reserves, wildlife management areas, and national parks. We classified anything not covered by these categories as unprotected (e.g. communal pastoral land, private land). We rasterized the two categories to the binary raster *protection status* (1 = protected, 0 = unprotected) with a resolution of 250m x 250m.

A.3.3 Human Influence

We created a raster layer representing human influence by integrating information on (1) human density, (2) farming, and (3) roads.

(1) We obtained spatial human density estimates through a publicly available 30m x 30m high-resolution population density dataset (`www.dataforgood.fb.com`; Facebook, 2019). We coarsened the layer to 250m x 250m by summing up human density values within each 250m x 250m cell.

(2) We sourced spatial information on farms from the Globeland (Chen et al., 2015) and Cropland (Xiong et al., 2017) land cover datasets from which we retained areas that were classified as either *cultivated land* or *croplands*. Any other land cover class was not pertinent to farming and therefore omitted. Because both layers had a resolution of 30m x 30m we coarsened them to 250m x 250m by assigning a value of 1 to any 250m x 250m cell that covered farmland and a value 0 otherwise. Thus, the final layer depicted presence (= 1) or absence (= 0) of farms within each 250m x 250m cell.

(3) We obtained geo-referenced data on roads from Open Street Map (Open Street Map, 2019), downloaded through Geofabrik (`www.geofabrik.de`). We only retained main tarmac roads and omitted smaller roads (Table S2) as these are scarcely frequented and do not represent an obstacle to wild dog movements (Abrahms et al., 2016). We

6

rasterized main tarmac roads to the binary raster *roads* (1 = roads, 0 = no roads) with 250m x 250m resolution. Finally, we created the covariate *distance to roads* by calculating the Euclidean distance of each raster cell in the study area to the nearest road.

Table S2: Description of road types, as sourced from Open Street Map's mapping guide (`https://wiki.openstreetmap.org/wiki/Key:highway`). Roads types that were considered for the purpose of this study are shaded in light gray.

Group	Subgroup	Description
Roads	motorway	A restricted access major divided highway, normally with 2 or more running lanes plus emergency hard shoulder. Equivalent to the Freeway, Autobahn, etc.
Roads	trunk	The most important roads in a country's system that aren't motorways. Need not necessarily be a divided highway.
Roads	primary	The next most important roads in a country's system. Often link larger towns.
Roads	secondary	The next most important roads in a country's system. Often link towns.
Roads	tertiary	The next most important roads in a country's system. Often link smaller towns and villages
Roads	unclassified	The least important thorough roads in a country's system, i.e. minor roads of a lower classification than tertiary, but which serve a purpose other than access to properties. Often link villages and hamlets.
Roads	residential	Roads which serve as an access to housing, without function of connecting settlements. Often lined with housing.
Roads	service	For access roads to, or within an industrial estate, camp site, business park, car park etc.
Link roads	motorway_link	The link roads (sliproads/ramps) leading to/from a motorway from/to a motorway or lower class highway. Normally with the same motorway restrictions.
Link roads	trunk_link	The link roads (sliproads/ramps) leading to/from a trunk road from/to a trunk road or lower class highway.
Link roads	primary_link	The link roads (sliproads/ramps) leading to/from a primary road from/to a primary road or lower class highway.
Link roads	secondary_link	The link roads (sliproads/ramps) leading to/from a secondary road from/to a secondary road or lower class highway.
Link roads	tertiary_link	The link roads (sliproads/ramps) leading to/from a tertiary road from/to a tertiary road or lower class highway.
Special road types	living_street	For living streets, which are residential streets where pedestrians have legal priority over cars, speeds are kept very low and where children are allowed to play on the street.
Special road types	pedestrian	For roads used mainly/exclusively for pedestrians in shopping and some residential areas which may allow access by motorised vehicles only for very limited periods of the day.
Special road types	track	Roads for mostly agricultural or forestry uses.
Special road types	bus_guideway	A busway where the vehicle is guided by the way (though not a railway) and is not suitable for other traffic.
Special road types	escape	For runaway truck ramps, runaway truck lanes, emergency escape ramps, or truck arrester beds. It enables vehicles with braking failure to safely stop.
Special road types	raceway	A course or track for racing
Special road types	road	A road/way/street/motorway/etc. of unknown type. It can stand for anything ranging from a footpath to a motorway.

Because layers (1), (2), and (3) depicted features that are typically spatially clustered and because not all dispersing coalitions moved within meaningful distance to each of these features, we totaled values from the layers describing *human density* (continuous), *farming* (binary), and *roads* (binary). This approach implied that *roads* and *farms* entered the final layer with a value of 1, whereas human density entered the final layer with a value ≥ 0 and potentially unbound. To reduce the influence of outliers in human density estimates, totaled values were limited to a maximum of 50, which visually resulted in a good balance

between high and low anthropogenic influence and was therefore considered appropriate for our analysis. To render the fact that humans influence their surroundings beyond their presence, we followed Elliot et al. (2014) and applied to each raster-cell a 5km focal buffer within which we summed up and log-transformed human-influence values.
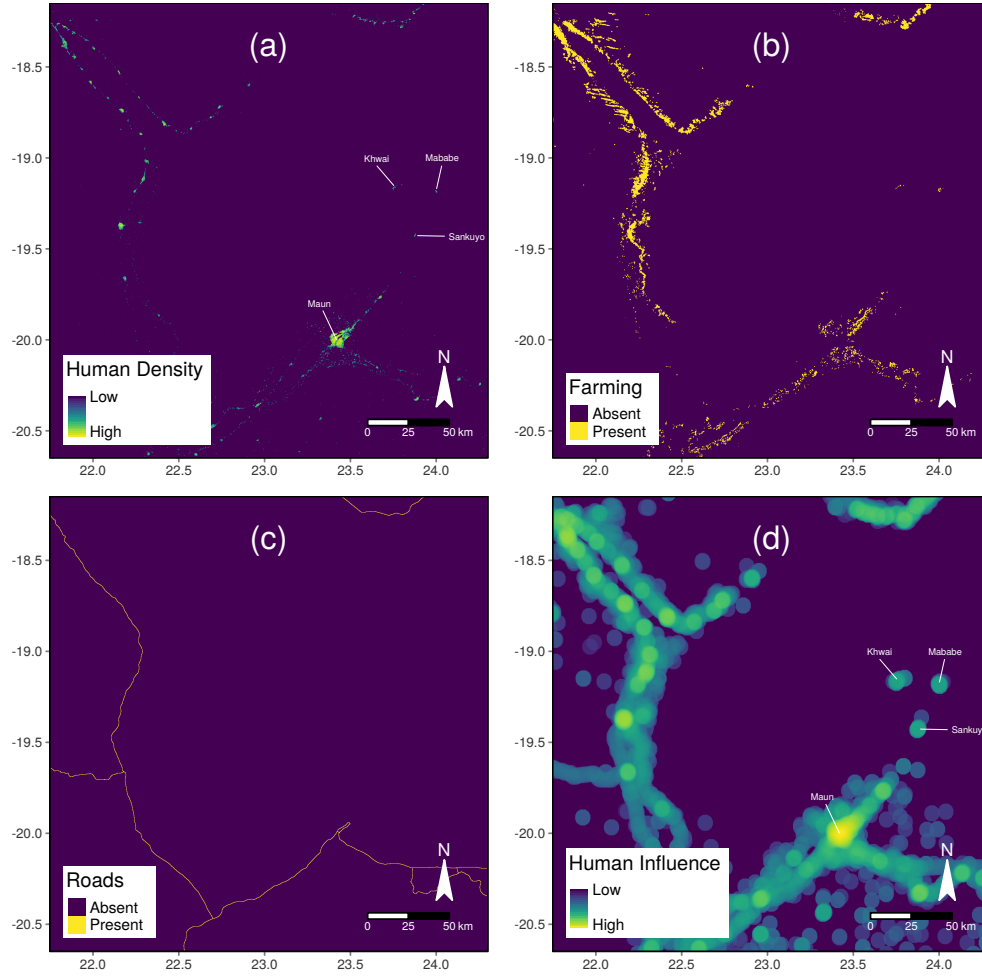

Figure S5: Sequence of figures that exemplifies how we combined the layers (a), (b), and (c) into a single layer for human influence (d). For better visibility we show the procedure only for the extent of the Okavango Delta. The layer in (a) is based on Facebook's high resolution human density dataset (`www.dataforgood.fb.com`; Facebook, 2019) and depicts the estimated number of humans living in each 250m x 250m raster-cell (coarsened from 30m x 30m). The layer in (b) is a binary layer and shows whether raster-cells are cover any sort of agricultural fields. Corresponding data was obtained through the Globeland and Cropland land cover datasets (Chen et al., 2015; Xiong et al., 2017). The layer in (c) shows the presence or absence of roads and is based on data from Open Street Map (Open Street Map, 2019). We merged the layers in (a), (b), and (c) by summing up their values, truncating the summed values to a maximum of 50. We then log-transforming the values and applied to each raster cell a focal buffer of 5km within which we totaled human influence values. The layer in (d) depicts the final human influence layer that entered our habitat selection model.
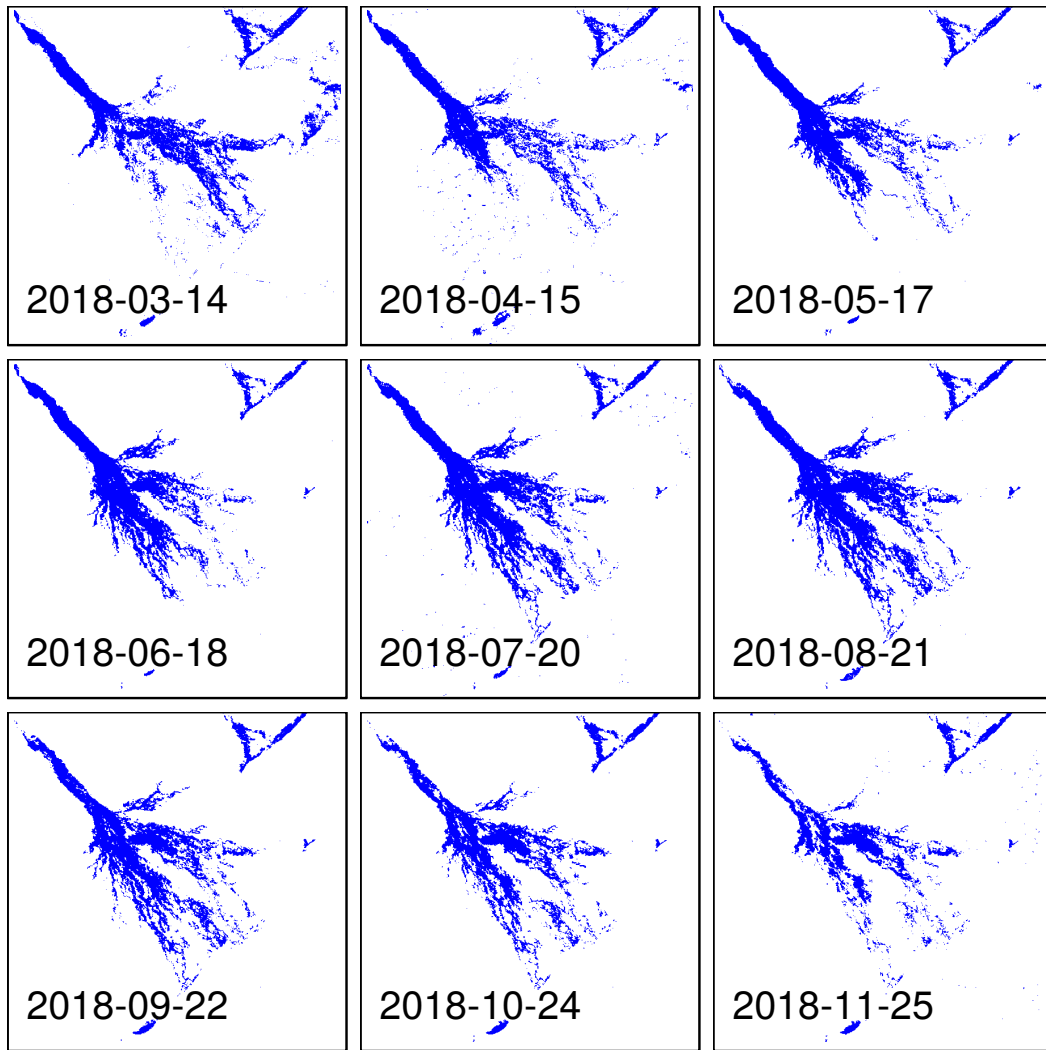
A.4   Typical Flood Pulse

Figure S6: Sequence of flood maps showing a typical flood pulse throughout the year. The flood arrives from the north-western corner (so called "pan-handle") of the Okavango Delta and slowly descends through the delta in south-eastern direction, where it nourishes several tributaries. The extent of the flood peaks around August or September and then slowly retracts. Between December and March the reflectance properties of water and dryland change, which is why often no accurate flood maps can be obtained for these months using remote sensing techniques (Wolski et al., 2017).

A.5 Integrated Step Selection Function

We used an integrated step selection function (iSSF; Avgar et al., 2016) to investigate dispersers' selection or avoidance of spatial covariates. In the iSSF framework, covariates experienced along realized steps are contrasted with covariates experienced along alternative random steps that the animal could have taken but decided not to. A step in this framework is defined as the connecting line between two consecutive GPS relocations (Turchin, 1998). In contrast to regular SSFs, iSSFs require to include movement metrics as covariates in the corresponding conditional logistic regression model. Their inclusion, in turn, allows simultaneous inference on habitat and movement preferences, as well as to reduce potential biases in estimated habitat preferences (Forester et al., 2009; Warton and Aarts, 2013; Avgar et al., 2016).

To conduct iSSF analysis, we followed the recommendations described in Appendix S1 of the publication by Avgar et al. (2016). We prepared our GPS relocation data for iSSF-analysis using the R-package *amt* (Signer et al., 2019) and coerced relocations recorded during dispersal to steps that were regularly spaced four hours apart. Steps that were separated by more than four hours (e.g. due to GPS failure) were omitted from further analysis (allowing for a minor mismatch of up to 15 minutes). Each remaining step was paired with 24 random steps, generated by sampling turning angles from a uniform distribution $U(-\pi, \pi)$ and step lengths from a gamma distribution that was fitted using realized step lengths (shape = 0.3677, scale = 6'302). Together, a realized and its 24 associated random steps formed a stratum of 25 steps that received a unique identifier.

We extracted spatial covariates along realized and random steps (Table S3). For continuous covariates, we calculated the average value, for categorical covariates the percentage cover along the step. We further derived a binary variable indicating whether a step crossed a road. We square-rooted extracted values to render a decreasing marginal impact of distance. We scaled covariates using a z-score transformation and screened for correlation using Pearson's Correlation Coefficient. None of the covariates were overly correlated ($|r| > 0.6$; Latham et al., 2011) and we retained all of them for modeling. Despite the covariates mentioned in Table S3, we included two movement metrics, namely the cosine of the turning angle ($cos(ta)$) and the logarithm of the step length ($log(sl)$) in our regression model (Avgar et al., 2016). The movement metric $cos(ta)$ serves to describe the directionality of a step, as it transforms the circular measure of ($-\pi$ to π) into a linear measure (-1, 1). Thus, positive values indicate forward movements, whereas negative values indicated backward movements (Turchin, 1998). The movement metric $log(sl)$, on the other hand, is as an indicator of the

10

157 preferred step length. Since in our case steps were spaced by four hours, $log(sl)$ can also be

158 interpreted as movement rate.

Table S3: Overview of spatial covariates and their sources. We extracted covariates along realized and random steps. For continuous covariates we calculated average values along steps, for categorical covariates the percentage coverage along steps. We also prepared two covariates indicating the distance to water and distance to roads, respectively. We square-rooted the values for these two covariates to render a decreasing marginal impact of the effect of distance. Finally, we derived a binary indicator of whether a step crossed a road or not.

Category	Covariate	Description	Values	Source
Land Cover	Water	Percentage cover of water	0-100%	(1) (2) (3)
	Dryland*	Percentage cover of dryland	0-100%	(1) (2) (3)
	DistanceToWater	Average distance to nearest water source	$\geq$ 0m	(1) (2) (3)
	Shrubs/Grassland	Average non-tree vegetation	0-100%	(4)
	Trees	Average tree-vegetation	0-100%	(4)
	Bareland*	Average non-vegetated area	0-100%	(4)
Protection Status	Protected	Percentage cover of protected area	0-100%	(5)
	Unprotected*	Percentage cover of unprotected area	0-100%	(5)
Human Influence	Human Influence	Average human influence	$\geq$ 0	(1) (6) (7) (8)
	DistanceToRoads	Average distance to nearest road	$\geq$ 0m	(1) (6) (7) (8)
	RoadCrossing	Binary; whether a step crossed a road	0, 1	(1) (6) (7) (8)

Sources: (1) Chen et al. (2015) (2) Schaaf and Wang (2015) (3) Yamazaki et al. (2019) (4) Dimiceli et al. (2015) (5) Peace Parks Foundation (2019) (6) Facebook (2019) (7) Open Street Map (2019) (8) Xiong et al. (2017)

* Note: The covariates *Water* and *Dryland* added up to 100%, which is why only *Water* was included as explanatory variable in our models. The same applied for the group *Shrubs/Grassland*, *Trees*, and *Bareland*, where we omitted *Bareland* for modeling. Finally, from the group *Protected* and *Unprotected*, we only included *Protected* in our models.

159 We then used the iSSF framework to parameterize a habitat selection model that further

160 served to predict landscape permeability. This habitat selection model operated under

161 the assumption that dispersing wild dogs assigned a selection score $w(x)$ of the following

162 exponential form to each realized and random step:

$$w(x) = exp(\beta_1 x_1 + \beta_2 x_2 + ... + \beta_n x_n) \qquad \text{(Equation S2)}$$

163 That is, the selection score $w(x)$ of a step depended on its associated covariates $(x_1, x_2, ..., x_n)$,

164 as well as on the animal's preferences for these covariates $(\beta_1, \beta_2, ..., \beta_n)$. The probability

165 that a step i was realized $P(Y_i = 1)$ was then contingent on the step's selection score, as

166 well as on the selection scores of all alternative steps in the stratum:

$$P(Y_i = 1 | Y_1 + Y_2 + ... + Y_i = 1) = \frac{w(x_i)}{w(x_1) + w(x_2) + ... + w(x_i)} \qquad \text{(Equation S3)}$$

167 Habitat and movement preferences of interest, i.e. the β's, were then estimated by compar-

168 ing realized (scored 1) and random (scored 0) steps in a conditional logistic regression model

169 (Fortin et al., 2005). In this model, positive β-coefficients indicate selection of a covariate,

170 negative β-coefficients avoidance of a covariate. To deal with multiple individuals, we ap-

plied mixed effects conditional logistic regression analysis following Muff et al. (2020). We implemented their method using the R-package *glmmTMB* (Brooks et al., 2017) and used dispersing coalition ID to model random intercepts and slopes.

We defined the movement metrics $cos(ta)$ and $log(sl)$ as core covariates and ran forward model selection based on Akaike's Information Criterion (AIC; Burnham and Anderson, 2002) for all other covariates. We ranked models according to AIC, assessed relative model weights, and identified the most parsimonious model. Due to convergence issues, we were unable to model interactions between covariates.

To validate the predictive power of the most parsimonious habitat selection model, we ran k-fold cross-validation for case-control studies as described in Fortin et al. (2009). Using 80% of randomly selected strata, we parameterized a habitat selection model and predicted selection scores $w(x)$ for all steps in the remaining 20% of strata. According to predicted selection scores we assigned ranks 1-25 within each stratum, with rank 1 indicating the highest selection score. We identified the realized step's rank in each stratum and tallied rank frequencies of realized steps across all strata. Finally, we carried out a Spearman-rank correlation analysis between ranks and associated frequencies and we recorded the correlation coefficient ($r_{s,realized}$). We repeated this procedure 100 times with replacement and computed the mean correlation coefficient ($\bar{r}_{s,realized}$), as well as its 95% confidence interval. For comparison, we also repeated the same procedure 100 times assuming completely randomized preferences. We implemented randomized preferences by omitting the realized step from each stratum and identifying the rank of a randomly chosen random step within each stratum (now only ranks 1-24). Again, we calculated Spearman's rank correlation coefficient ($r_{s,random}$), its mean across repetitions ($\bar{r}_{s,random}$), and its 95% confidence interval. Ultimately, the validation proved a significant prediction in case the confidence intervals of $\bar{r}_{s,realized}$ and $\bar{r}_{s,random}$ did not overlap.

A.6 Identification of Least-Cost Paths & Corridors

A.6.1 Least-Cost Paths

We implemented factorial LCP analysis between source points using the R-package *gdistance* (Figure S.7; van Etten, 2017). The package translated the (unscaled) permeability surface into a network of nodes to find shortest effective distances between source points based on probabilities of moving from cell to cell. In our case, the transition probability of moving between two adjacent cells depended on their averaged permeability. We allowed individuals to move from each cell to the cell's eight surrounding neighbors (i.e. Moores neighborhood) and applied a geographic correction to account for the fact that diagonal neighbors were more remote than orthogonal neighbors. Because African wild dogs have been observed to cover large dispersal distances (Davies-Mostert et al., 2012; Masenga et al., 2016; Cozzi et al., 2020), we did not limit LCPs to a maximal effective cost. After computation, we tallied overlapping LCPs and identified high-frequency routes.

A.6.2 Least-Cost Corridors

We calculated factorial LCCs (Pinto and Keitt, 2009; Sawyer et al., 2011; Elliot et al., 2014), again using the R-package *gdistance* (Figure S.7; van Etten, 2017). To identify LCCs, we first computed for each source point a cumulative cost map, which indicated the total minimal costs required to get from the source point to any other location in the study area. We then obtained an LCC between two source points by adding up their cumulative cost maps and masking out all cell-values exceeding the lowest cell-value by more than 5% (Pinto and Keitt, 2009). We repeated this procedure for each possible unique pairwise combination of source points and thereby identified LCCs between all 68 selected source points. We normalized the resulting corridor-maps to range from zero to one and tallied them into a single connectivity map.
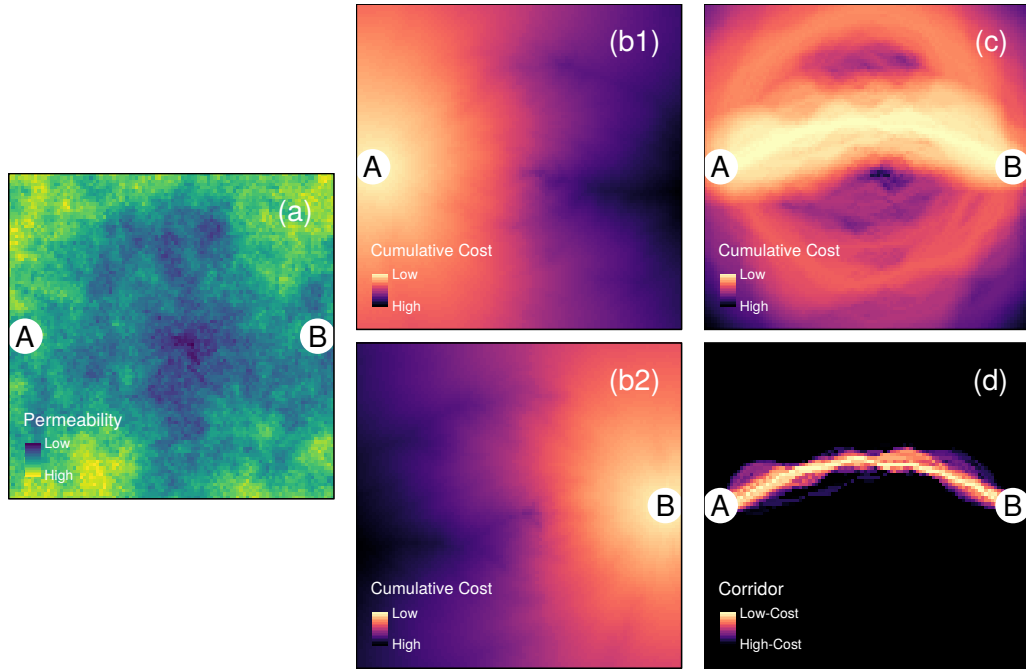
Figure S7: Images illustrating the process of identifying a least-cost corridor between source points A and B following Pinto and Keitt (2009). (a) Example of a permeability surface, which determines the costs of movement. (b1) Cumulative cost map for point A, depicting the total minimal costs necessary to get from point A to every other location. (b2) Cumulative cost map for point B, depicting the total minimal costs to get from point B to every other location. (c) Summed cost maps of points A and B. (d) Masked out corridor containing pixels that do not exceed the cheapest pixel by more than 5%.

A.7 Model Selection Results

Table S4: Results from the forward model selection procedure based on Akaike's Information Criterion (AIC; Burnham and Anderson, 2002) for the habitat selection model. The most parsimonious model outperformed all other models ($\Delta AIC > 2$) and received a weight of one.

Covariates	AIC	ΔAIC	Weight	LogLik
cos(ta) + log(sl) + W + T + DTW + HI + S	90091.40	0.00	1.00	-45030.70
cos(ta) + log(sl) + W + T + DTW + HI + S + DTR	90093.51	2.11	0.00	-45029.75
cos(ta) + log(sl) + W + T + DTW + HI	90094.79	3.38	0.00	-45034.39
cos(ta) + log(sl) + W + T + DTW + HI + S + P	90095.05	3.65	0.00	-45030.52
cos(ta) + log(sl) + W + T + DTW + S	90096.95	5.55	0.00	-45035.47
cos(ta) + log(sl) + W + T + DTW + HI + DTR	90097.02	5.62	0.00	-45033.51
cos(ta) + log(sl) + W + T + DTW + HI + S + DTR + P	90097.38	5.98	0.00	-45029.69
cos(ta) + log(sl) + W + T + DTW + HI + S + RC	90097.53	6.13	0.00	-45029.76
cos(ta) + log(sl) + W + T + DTW + HI + P	90098.46	7.06	0.00	-45034.23
cos(ta) + log(sl) + W + T + DTW + HI + S + DTR + RC	90099.62	8.22	0.00	-45028.81
cos(ta) + log(sl) + W + T + DTW	90099.97	8.57	0.00	-45038.99
cos(ta) + log(sl) + W + T + DTW + HI + RC	90100.68	9.28	0.00	-45033.34
cos(ta) + log(sl) + W + T + DTW + DTR	90101.68	10.28	0.00	-45037.84
cos(ta) + log(sl) + W + T + DTW + P	90103.07	11.67	0.00	-45038.54
cos(ta) + log(sl) + W + T + DTW + HI + S + DTR + P + RC	90103.48	12.08	0.00	-45028.74
cos(ta) + log(sl) + W + T + DTW + RC	90104.72	13.32	0.00	-45037.36
cos(ta) + log(sl) + W + T + HI	90123.71	32.31	0.00	-45050.85
cos(ta) + log(sl) + W + T	90128.17	36.77	0.00	-45055.09
cos(ta) + log(sl) + W + T + S	90129.36	37.96	0.00	-45053.68
cos(ta) + log(sl) + W + T + DTR	90130.11	38.71	0.00	-45054.05
cos(ta) + log(sl) + W + T + P	90131.75	40.35	0.00	-45054.88
cos(ta) + log(sl) + W + T + RC	90133.53	42.13	0.00	-45053.77
cos(ta) + log(sl) + W + DTW	90138.92	47.52	0.00	-45060.46
cos(ta) + log(sl) + W + HI	90149.30	57.90	0.00	-45065.65
cos(ta) + log(sl) + W + S	90151.14	59.74	0.00	-45066.57
cos(ta) + log(sl) + W	90153.70	62.30	0.00	-45069.85
cos(ta) + log(sl) + W + DTR	90156.32	64.92	0.00	-45069.16
cos(ta) + log(sl) + W + P	90157.23	65.83	0.00	-45069.62
cos(ta) + log(sl) + W + RC	90159.32	67.91	0.00	-45068.66
cos(ta) + log(sl) + S	90161.07	69.67	0.00	-45073.54
cos(ta) + log(sl) + DTW	90262.03	170.63	0.00	-45124.01
cos(ta) + log(sl) + T	90301.56	210.16	0.00	-45143.78
cos(ta) + log(sl) + HI	90307.55	216.15	0.00	-45146.78
cos(ta) + log(sl) + DTR	90316.37	224.97	0.00	-45151.19
cos(ta) + log(sl) + P	90316.62	225.22	0.00	-45151.31
cos(ta) + log(sl) + RC	90318.46	227.06	0.00	-45150.23

Note: W = Water, DTW = Distance To Water, S = Shrubs/Grassland, T = Trees, P = Protected, HI = Human Influence, RC = Road Crossing, DTR = Distance To Roads.

References

Abrahms, B., Jordan, N. R., Golabek, K. A., McNutt, J. W., Wilson, A. M., and Brashares, J. S. (2016). Lessons from Integrating Behaviour and Resource Selection: Activity-Specific Responses of African Wild Dogs to Roads. *Animal Conservation*, 19(3):247–255.

Avgar, T., Potts, J. R., Lewis, M. A., and Boyce, M. S. (2016). Integrated Step Selection Analysis: Bridging the Gap Between Resource Selection and Animal Movement. *Methods in Ecology and Evolution*, 7(5):619–630.

Brooks, M. E., Kristensen, K., van Benthem, K. J., Magnusson, A., Berg, C. W., Nielsen, A., Skaug, H. J., Maechler, M., and Bolker, B. M. (2017). glmmTMB Balances Speed and Flexibility among Packages for Zero-Inflated Generalized Linear Mixed Modeling. *The R Journal*, 9(2):378–400.

Burnham, K. P. and Anderson, D. R. (2002). *Model Selection and Multimodel Inference: A Practical Information-Theoretic Approach*. Springer Science & Business Media, Ney York, NY, USA.

Chen, J., Chen, J., Liao, A., Cao, X., Chen, L., Chen, X., He, C., Han, G., Peng, S., and Lu, M. (2015). Global Land Cover Mapping at 30m Resolution: A POK-Based Operational Approach. *ISPRS Journal of Photogrammetry and Remote Sensing*, 103:7–27.

Cozzi, G., Behr, D. M., Webster, H. S., Claase, M., Bryce, C. M., Modise, B., Mcnutt, J. W., and Ozgul, A. (2020). African Wild Dog Dispersal and Implications for Management. *The Journal of Wildlife Management*, 84(4):614–621.

Davies-Mostert, H. T., Kamler, J. F., Mills, M. G. L., Jackson, C. R., Rasmussen, G. S. A., Groom, R. J., and Macdonald, D. W. (2012). Long–Distance Transboundary Dispersal of African Wild Dogs among Protected Areas in Southern Africa. *African Journal of Ecology*, 50(4):500–506.

Dimiceli, C., Carroll, M., Sohlberg, R., Kim, D., Kelly, M., and Townshend, J. (2015). MOD44B MODIS/Terra Vegetation Continuous Fields Yearly L3 Global 250m SIN Grid v006. *NASA EOSDIS Land Processes DAAC*. Accessed 2019-11-12 from `https://doi.org/10.5067/MODIS/MOD44B.006`.

Elliot, N. B., Cushman, S. A., Macdonald, D. W., and Loveridge, A. J. (2014). The Devil is in the Dispersers: Predictions of Landscape Connectivity Change with Demography. 51(5):1169–1178.

Facebook (2019). High Resolution Population Density Maps. Accessed 2019-11-12 from `https://data.humdata.org/dataset/highresolutionpopulationdensitymaps`.

Forester, J. D., Im, H. K., and Rathouz, P. J. (2009). Accounting for Animal Movement in Estimation of Resource Selection Functions: Sampling and Data Analysis. *Ecology*, 90(12):3554–3565.

Fortin, D., Beyer, H. L., Boyce, M. S., Smith, D. W., Duchesne, T., and Mao, J. S. (2005). Wolves Influence Elk Movements: Behavior Shapes a Trophic Cascade in Yellowstone National Park. *Ecology*, 86(5):1320–1330.

Fortin, D., Fortin, M.-E., Beyer, H. L., Duchesne, T., Courant, S., and Dancose, K. (2009). Group-Size-Mediated Habitat Selection and Group Fusion–Fission Dynamics of Bison under Predation Risk. *Ecology*, 90(9):2480–2490.

Latham, A. D. M., Latham, M. C., Boyce, M. S., and Boutin, S. (2011). Movement Responses by Wolves to Industrial Linear Features and Their Effect on Woodland Caribou in Northeastern Alberta. *Ecological Applications*, 21(8):2854–2865.

Masenga, E. H., Jackson, C. R., Mjingo, E. E., Jacobson, A., Riggio, J., Lyamuya, R. D., Fyumagwa, R. D., Borner, M., and Røskaft, E. (2016). Insights into Long-Distance Dispersal by African Wild Dogs in East Africa. *African Journal of Ecology*, 54(1):95–98.

Muff, S., Signer, J., and Fieberg, J. (2020). Accounting for Individual-Specific Variation in Habitat-Selection Studies: Efficient Estimation of Mixed-Effects Models Using Bayesian or Frequentist Computation. *Journal of Animal Ecology*, 89(1):80–92.

Open Street Map (2019). Planet dump retrieved from https://planet.osm.org. Accessed 2019-11-12 from `https://www.openstreetmap.org`.

Peace Parks Foundation (2019). SADC Protected Areas. Accessed 2019-11-12 from `http://new-ppfmaps.opendata.arcgis.com/datasets/ppf-protected-areas-detailed?geometry=-13.87,-25.558,69.846,-11.001`.

Pinto, N. and Keitt, T. H. (2009). Beyond the Least-Cost Path: Evaluating Corridor Redundancy Using a Graph-Theoretic Approach. *Landscape Ecology*, 24(2):253–266.

R Core Team (2019). *R: A Language and Environment for Statistical Computing*. R Foundation for Statistical Computing, Vienna, Austria.

Sawyer, S. C., Epps, C. W., and Brashares, J. S. (2011). Placing Linkages among Fragmented Habitats: Do Least-Cost Models Reflect How Animals Use Landscapes? *Journal of Applied Ecology*, 48(3):668–678.

Schaaf, C. and Wang, Z. (2015). MCD43A4 MODIS/Terra + Aqua BRDF/Albedo Nadir BRDF Adjusted RefDaily L3 Global - 500m v006. *NASA EOSDIS Land Processes DAAC*. Accessed 2019-11-12 from `https://doi.org/10.5067/MODIS/MCD43A4.006`.

Schwalb-Willmann, J. (2018). *getSpatialData: Get Different Kinds of Freely Available Spatial Datasets*. R package version 0.0.4.

Signer, J., Fieberg, J., and Avgar, T. (2019). Animal Movement Tools (amt): R Package for Managing Tracking Data and Conducting Habitat Selection Analyses. *Ecology and Evolution*, 9:880–890.

Turchin, P. (1998). *Quantitative Analysis of Movement: Measuring and Modeling Population Redistribution in Plants and Animals*. Sinauer Associates, Sunderland, MA, USA.

van Etten, J. (2017). *R Package gdistance: Distances and Routes on Geographical Grids*.

Warton, D. and Aarts, G. (2013). Advancing our Thinking in Presence-Only and Used-Available Analysis. *Journal of Animal Ecology*, 82(6):1125–1134.

Wolski, P., Murray-Hudson, M., Thito, K., and Cassidy, L. (2017). Keeping it Simple: Monitoring Flood Extent in Large Data-Poor Wetlands Wsing MODIS SWIR Data. *International Journal of Applied Earth Observation and Geoinformation*, 57:224–234.

Xiong, J., Thenkabail, P., Tilton, J., Gumma, M., Teluguntla, P., Oliphant, A., Congalton, R., Yadav, K., and Gorelick, N. (2017). Nominal 30m Cropland Extent Map of Continental Africa by Integrating Pixel-Based and Object-Based Algorithms Using Sentinel-2 and Landsat-8 Data on Google Earth Engine. *Remote Sensing*, 9(10):1065.

Yamazaki, D., Ikeshima, D., Sosa, J., Bates, P. D., Allen, G. H., and Pavelsky, T. M. (2019). MERIT Hydro: A High-Resolution Global Hydrography Map Based on Latest Topography Dataset. *Water Resources Research*, 55(6):5053–5073.